Measured and Predicted Turbulent Kinetic Energy in Flow Through Emergent Vegetation With Real Plant Morphology

Citation: Xu, Y., & Nepf, H. (2020). Measured and predicted turbulent kinetic energy in flow through emergent vegetation with real plant morphology. Water Resources Research, 56, e2020WR027892

As Published: 10.1029/2020WR027892

Publisher: American Geophysical Union (AGU)

Persistent URL: https://hdl.handle.net/1721.1/133055

Version: Final published version: final published article, as it appeared in a journal, conference proceedings, or other formally published context

Water Resources Research

RESEARCH ARTICLE
10.1029/2020WR027892

Measured and Predicted Turbulent Kinetic Energy in Flow Through Emergent Vegetation With Real Plant Morphology

Yuan Xu[1,2] **and Heidi Nepf**[1]

[1]Department of Civil and Environmental Engineering, MIT, Cambridge, MA, USA, [2]State Key Laboratory of Hydroscience and Engineering, Tsinghua University, Beijing, China

Abstract Velocity and forces on individual plants were measured within an emergent canopy with real plant morphology and used to develop predictions for the vertical profiles of velocity and turbulent kinetic energy (*TKE*). Two common plant species, *Typha latifolia* and *Rotala indica*, with distinctive morphology, were considered. *Typha* has leaves bundled at the base, and *Rotala* has leaves distributed over the length of the central stem. Compared to conditions with a bare bed and the same velocity, the *TKE* within both canopies was enhanced. For the *Typha* canopy, for which the frontal area increased with distance from the bed, the velocity, integral length-scale, and *TKE* all decreased with distance from the bed. For the *Rotala*, which had a vertically uniform distribution of biomass, the velocity, integral length-scale, and *TKE* were also vertically uniform. A turbulence model previously developed for random arrays of rigid cylinders was modified to predict both the vertical distribution and the channel-average of *TKE* by defining the relationship between the integral length-scale and plant morphology. The velocity profile can also be predicted from the plant morphology. Combining with the new turbulence model, the *TKE* profile was predicted from the channel-average velocity and plant frontal area.

Key Points:
- Within an emergent canopy, vertical profiles of velocity and *TKE* vary inversely with the vertical distribution of plant frontal area
- A turbulence model for cylinders was modified to predict the vertical-distribution and the channel-average of *TKE*
- *TKE* profiles can be predicted from the channel-average velocity and the vertical distribution of plant frontal area

Supporting Information:
- Supporting Information S1

Correspondence to:
Y. Xu,
xuyuan18@mails.tsinghua.edu.cn

Citation:
Xu, Y., & Nepf, H. (2020). Measured and predicted turbulent kinetic energy in flow through emergent vegetation with real plant morphology. *Water Resources Research*, *56*, e2020WR027892. https://doi.org/10.1029/2020WR027892

Received 6 MAY 2020
Accepted 2 NOV 2020
Accepted article online 9 NOV 2020

1. Introduction

In rivers, streams, lakes, and coastal regions, aquatic vegetation provides a wide range of ecosystem services, including enhancing water quality, sheltering economically important fish, and stabilizing the bed (e.g., Barbier et al., 2011; Costanza et al., 1997; Kemp et al., 2000; Wilcock et al., 1999). The vegetation produces an additional drag force that shapes the mean and turbulent velocity profiles (e.g., Liu et al., 2018; Nepf, 1999; Stoesser et al., 2010; Tsujimoto, 1999), which in turn influences sediment transport and channel morphology (e.g., Bennett et al., 2008; Corenblit et al., 2007; Rominger et al., 2010). Enhanced deposition within regions of vegetation stabilizes the channel bed and facilitates the expansion of the vegetated region (e.g., Gurnell, 2014). Finally, the reduced velocity within vegetation provides important fish habitat (Lenhart, 2008; Montakhab et al., 2012). Given the importance of vegetation in shaping and enhancing aquatic landscapes, many studies have sought a better understanding of the interaction between flow and vegetation. In particular, this study examined how vegetation with real, nonuniform morphology shapes the channel turbulence.

Several researchers have measured the vegetation-generated turbulence in the laboratory and in the field and illustrated the role of turbulence in environmental transport. Vegetation-generated turbulence can enhance nutrient uptake by vegetation (e.g., Cornacchia et al., 2018: Morris et al., 2008). Vegetation-generated turbulence has also been observed to promote sediment resuspension and bed load transport, leading to sediment mobilization at lower velocity than observed for bare bed (Hongwu et al., 2013; Tinoco & Coco, 2016, 2018; Wang et al., 2015; Yager & Schmeeckle, 2013; Yang et al., 2016). Several studies have measured reduced turbulence levels within marsh canopies, compared to adjacent channels, and associated it with the enhanced deposition (Christiansen et al., 2000; Leonard & Croft, 2006; Neumeier, 2007). Finally, vegetation-generated turbulence enhances the turbulent diffusivity within a canopy, which in turn can influence the distribution of suspended sediment within the water column (Huai et al., 2019; Li et al., 2020; Termini, 2019). These studies reveal the importance of vegetation-generated turbulence, and the goal of this study is to provide a more accurate method to predict it.

Previous studies have constructed models to predict and/or simulate the turbulence generated by vegetation (e.g., King et al., 2012; López & García, 1998; Stoesser et al., 2010; Uittenbogaard, 2003). The majority of these studies represented the vegetation canopy with an array of rigid, circular cylinders, for which the frontal area of the model and the integral length scale of the turbulence are both uniform over depth. However, King et al. (2012) noted that for real plants, whose geometry is more complex than a rigid cylinder, the integral length scale can vary over the depth of the flow. Similarly, measurements in a model mangrove forest found two different scales of turbulence generated by the near-bed region occupied by roots and the upper region occupied by trunks (Maza et al., 2017). To complement this previous work, the present study measured the velocity and *TKE* within a canopy consisting of plastic vegetation with morphology identical to the real plant species *Typha latifolia* and *Rotala indica* and constructed a model to predict the *TKE* generated by these plants. These species were selected for their contrasting morphology. Specifically, *Typha* has leaves bundled at the base, and *Rotala* has leaves distributed over the length of a central stem. With regard to the vertical profile of frontal area, *Typha* has a nonuniform distribution and *Rotala* has a uniform distribution. We note that under some flow conditions, aquatic plants exhibit reconfiguration (bending) in response to flow (e.g., Sand-Jensen, 2003; Vogel, 1989) and that reconfiguration typically reduces the vegetation drag (e.g., de Langre et al., 2012; Fathi-Maghadam & Kouwen, 1997; Harder et al., 2004) but can sometime increase the drag (Zhang & Nepf, 2020), both of which would impact vegetation-generated turbulence. However, reconfiguration was not considered in this study, and for the flow and depth conditions considered here, the model plants did not reconfigure. The theory behind the turbulence model is described in section 2. Section 3 describes the geometry of the plants and the measurements of velocity and drag force. Section 4 reports the results for *Typha* and *Rotala* plants and compares measured and predicted *TKE*. Finally, using a momentum-based model to predict velocity, the *TKE* within the *Typha* canopy was predicted from just the channel-average velocity and the vegetation morphology.

2. Theory

At the scale of a wetland, river, or coastal ocean, it is not practical to resolve the flow field at the scale of each plant. To capture the impact of the vegetation on the larger-scale dynamics, Wilson and Shaw (1977) and Raupach and Shaw (1982) described a double-averaging method that first takes a time average to smooth over fluctuations due to small-scale turbulence and then takes an average over a horizontal plane to eliminate heterogeneity due to the canopy structure. Because the spatial average is over the horizontal plane, it preserves vertical variation in plant biomass. Specifically, a scalar field Ψ (such as pressure, temperature, or streamwise velocity component) is represented as

$$\Psi = \overline{\Psi} + \Psi', \tag{1}$$

$$\overline{\Psi} = \langle \overline{\Psi} \rangle + \overline{\Psi}'', \tag{2}$$

in which overbars and brackets denote the temporal and horizontal averages, respectively; and the single and double primes indicate the fluctuation from temporal and horizontal averages, respectively. x, y, and z are Cartesian coordinates. The x-axis is aligned with the direction of the mean flow. The y-axis is the horizontal, span-wise direction, and the z-axis is vertical, with $z = 0$ at the bed, and positive upward. The instantaneous velocity u, v, and w correspond to the directions x, y, and z, respectively.

The double-averaged governing equation for *TKE* in steady, uniform, fully developed flow is

$$\frac{\partial k_t}{\partial t} = 0 = T + P_s + P_w - \varepsilon, \tag{3}$$

with

$$T = \frac{\partial}{\partial Z}\left[-\frac{\langle \overline{u'_i u'_i w'} \rangle}{2} - \frac{\langle \overline{p' w'} \rangle}{\rho} + \nu \left\langle \overline{u'_i \left(\frac{\partial u'_i}{\partial z} + \frac{\partial w'}{\partial x_i} \right)} \right\rangle - \frac{\left\langle \overline{u'_i u'_i}'' \overline{w}'' \right\rangle}{2}\right], \tag{4}$$

$$P_s = -\langle \overline{u'w'} \rangle \frac{\partial \langle \overline{u} \rangle}{\partial z}, \tag{5}$$

$$P_w = -\left\langle \overline{u'_i u'_j}'' \frac{\partial \overline{u}_i''}{\partial x_j} \right\rangle, \tag{6}$$

in which k_t is the turbulent kinetic energy, T represents the transport terms, P_s and P_w are the shear production and wake production, respectively, and ε is the rate of viscous dissipation. The first three terms in Equation 4 denote turbulent, pressure, and molecular transport, respectively. The fourth term, the dispersive transport, arises from spatial correlations in the time-mean velocity field. A detailed discussion of each term can be found in Raupach and Shaw (1982) and Nikora et al. (2007).

Starting from the *TKE* budget (Equation 3), Tanino and Nepf (2008) predicted the *TKE* within an array of vertical, emergent cylinders of diameter d, for which the wake production far exceeds the shear production, and the transport terms are negligible, such that the turbulent kinetic energy budget reduces to a balance between the wake production and the viscous dissipation (King et al., 2012; Nepf & Vivoni, 2000; Tanino & Nepf, 2008),

$$P_w \approx \varepsilon. \tag{7}$$

If the scale of the canopy elements d (cylinder diameter) is much larger than the Kolmogorov microscale η, the dissipation of mean kinetic energy due to viscous drag is negligible compared to that due to form drag (López & García, 2001; Raupach & Shaw, 1982; Tanino & Nepf, 2008), in which case the wake production can be assumed to equal the rate of work done by the mean flow against the canopy form drag, that is,

$$P_w \approx \langle \overline{u} \rangle f_i^{form} = \frac{1}{2} \frac{C_D^{form} a}{(1-\phi)} \langle \overline{u} \rangle^3. \tag{8}$$

Only the form drag, f_i^{form}, represented with drag coefficient C_D^{form} is considered in 8, because the viscous component of drag is dissipated to heat. Here, a is the frontal area per unit canopy volume, and ϕ is the solid volume fraction within the canopy. The rate of turbulent energy dissipation, ε, scales with the characteristic eddy length scale, l_t (Tennekes & Lumley, 1972),

$$\varepsilon \sim \frac{k_t^{3/2}}{l_t}. \tag{9}$$

Combining Equations 7, 8, and 9, Tanino and Nepf (2008) predicted the turbulence intensity within an array of emergent cylinders,

$$k_t = \gamma^2 \left(C_D^{form} \frac{a l_t}{2(1-\phi)} \right)^{2/3} U^2, \tag{10}$$

in which γ is an empirical constant, and $U = Q/(WH(1-\phi))$ is the channel-average velocity. Q is channel discharge, W is the channel width, H is the water depth, and ϕ is the fraction of canopy volume occupied by plants. By definition, $U = \langle \overline{u} \rangle$. While Tanino and Nepf (2008) provide estimates of C_D^{form}, in general, it is difficult to measure directly. However, numerical results by Etminan et al. (2018) suggest that for $Ud/\nu > 200$, the form drag constitutes 90% of the total drag for bluff objects. Therefore, it is reasonable to approximate $C_D^{form} \approx C_D$, in which C_D is the total measured drag coefficient.

In an array of emergent cylinders, the length-scale l_t is equal to the cylinder diameter d, if the mean surface-to-surface spacing, s, is larger than d, which simplifies Equation 10 (this study) to Equation 2.9 in Tanino and Nepf (2008). However, for canopies of more complex morphology, the scale for l_t is not obvious. A goal of this study was to modify Equation 10 to predict *TKE* within an emergent canopy of *Typha* and *Rotala* plants. First, the varied morphology of real plants generates vertical shear and possibly shear production. However, a comparison of shear production and stem production verified that $P_s \ll P_w$. Second, force measurements were used to estimate the drag coefficient for individual plants within the canopy. Third,

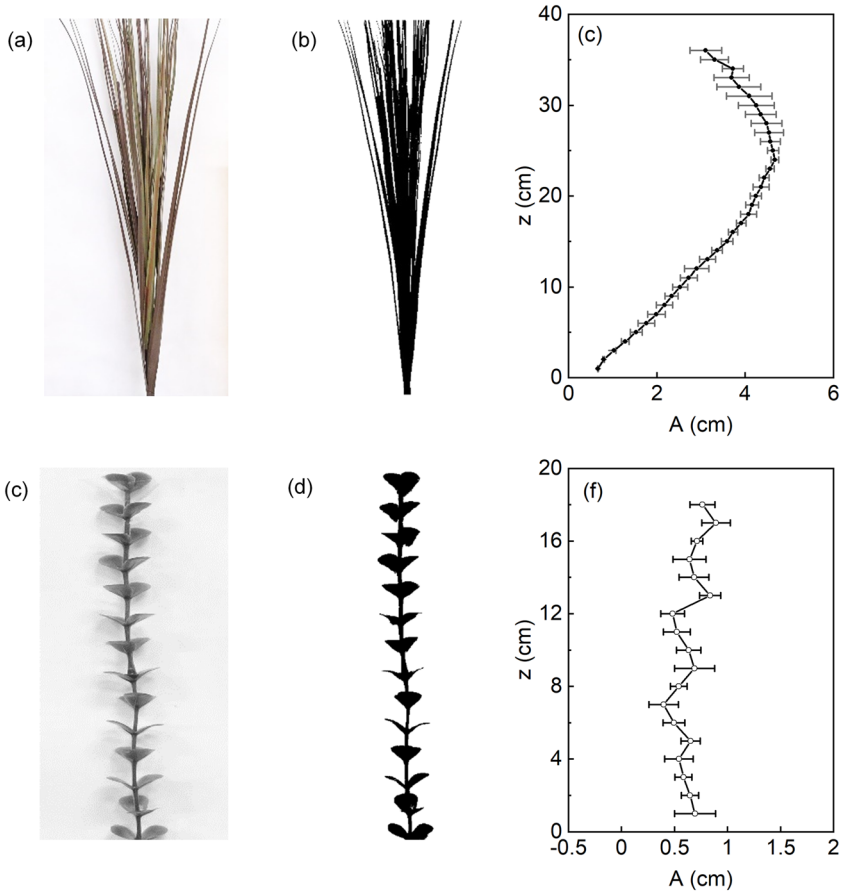

Figure 1. Original image of (a) *Typha latifolia* and (d) *Rotala indica*; (b) and (e) conversion of original image to a binary image; (c) and (f) the vertical profiles of plant frontal area per cm vertical interval, A [cm^2/cm], for *Typha* and *Rotala*, respectively. The error bars indicate the variability associated with nine difference images representing three different orientations of three different plants.

measurements of the integral length-scale were used to define an appropriate predictor of l_t. Finally, these steps were combined to develop and validate a prediction of spatially-averaged *TKE* within emergent stands of *Typha* and *Rotala*.

3. Methods

3.1. Plant Morphology

The common wetland plant, *Typha latifolia*, consists of long sword-shaped leaves, which are bundled into a culm at the base (Figure 1a). Each plastic plant consisted of 40 leaves, with length $l_1 = 30$ to 40 cm and width $w_1 = 0.1$ to 0.4 cm, which is the same as real *Typha* leaves (Liu et al., 2017). The frontal area of a *Typha* plant has significant vertical variation. For comparison, a second plant with a uniform distribution of biomass, *Rotala indica*, was also considered (Figure 1d). Each *Rotala* plant consisted of an 18-cm stem with a diameter of 0.2 cm and 28 oval leaves, $l_2 = 1.2$ cm in length and $w_2 = 1.1$ cm in width. Both plants were made of flexible plastic, but for the range of velocity considered, neither model plant exhibited reconfiguration.

The frontal area of individual plants was measured using image analysis. Three randomly selected plants of each species were photographed against a white background with a vertical ruler. For each plant, three photos were taken using three different angles of rotation (i.e., nine photos per species). The frontal area was estimated using a MATLAB image processing code to convert the original image into a binary file based on color thresholds (Figures 1b and 1e). The black pixels of the binary image were counted, and a conversion factor between pixels and length was determined using the reference ruler. The frontal area associated with

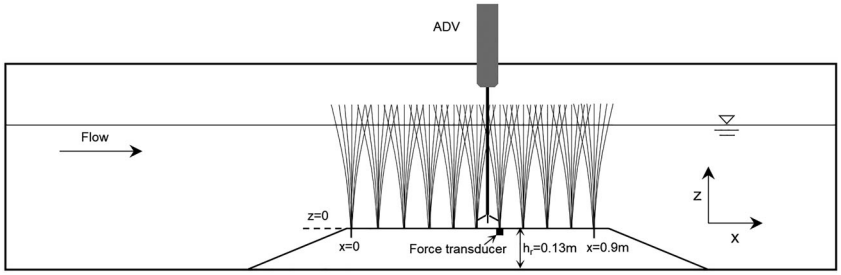

Figure 2. Schematic of flume viewed from side. The figure is not to scale. The length of the canopy is 0.9 m. The Nortek Vectrino is mounted on a mobile trolley (not shown) which allowed positioning within the canopy. The force transducer is mounted in an acrylic ramp that spanned the channel. The ramp is 13 cm high, 2 m long on the base, and 1 m long on top.

one plant within each 1-cm vertical interval, $A(z)[\mathrm{cm}^2/\mathrm{cm}]$, is shown in Figures 1c and 1f. The horizontal bars indicate the variability among different plants and orientations. The cumulative frontal area of one plant, A_f, was evaluated by integrating the curve $A(z)$ over the water depth. For a canopy with m plants per bed area, the frontal area per canopy volume was defined as $a(z)[cm^{-1}] = m\,A(z)$. For the *Typha* canopy, a varied with distance from the bed, but a was almost constant for the *Rotala* canopy.

3.2. Experimental Setup

The experiments were conducted in the Nepf Laboratory at MIT, in two recirculating channels (Figure 2). Experiments with shallow water depth (8–14 cm) were conducted in a 3.75-m and 0.40-m wide flume (hereafter referred as Flume 1). Experiments with large water depth (14–35 cm) were conducted in a 24-m long and 0.38-m wide flume (Flume 2). The bed slope of both flumes was zero. The canopy was constructed using model plants placed into a staggered arrangement in predrilled PVC baseboards (Figure 3a). Each baseboard was 1-m long, 0.35-m wide, and 6-mm high. The area density, m, of the *Typha* canopy differed slightly between the flumes due to differences in the baseboards. The value of m was 86 plants/m^2 in Flume 1 and 119 plants/m^2 in Flume 2. For the *Rotala* canopy, experiments were only conducted in Flume 2, with two area densities, m = 447 and 795 plants/m^2. The length of both canopies was 0.9 m. Plant characteristics are summarized in Table 1.

Flow discharge, Q, was controlled by a variable-speed pump and measured using a flow meter. The imposed flow was constant and uniform. Two rulers (located at $x = 0.1$ and 0.7 m, respectively) on the channel sidewall were used to measure the water depth H, which was evaluated from the top of the baseboard to the water surface. For the *Typha* canopy, six water depths ranging from 8 cm to 35 cm were considered. For the largest water depth, $H = 35$ cm, the plants were nearly submerged. For each water depth, four to seven different pump rates were selected, producing 28 cases. Each velocity and depth condition was repeated with only the PVC baseboards, that is, without vegetation. The channel-average velocity $U = Q/(WH(1-\phi))$ was

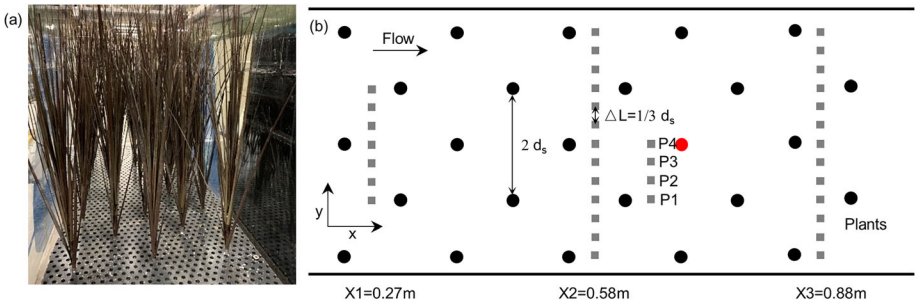

Figure 3. (a) Photograph of *Typha* canopy. (b) Schematic top view of *Typha* canopy. Black dots show the position of individual plants at the base. The red dot is the plant attached to the force transducer. Gray squares are ADV measurement locations. P1 to P4 are the positions in the unit cell. The spacing between plant rows is d_s, as shown in Table 1.

Table 1
Flow Characteristics and Vegetation Parameters

Run	H (cm)	$U \pm \sigma_U$ [a] (cm/s)	m (plants/m^2)	d_s [b] (cm)	$\langle a \rangle_z$ [c] (m^{-1})	ϕ	$\langle k_t \rangle_z \pm \boldsymbol{\sigma}_{k_t}$ [d] (cm^2/s^2)
Typha canopy							
1.1	8	4.5 ± 0.2	86	7.6	1.21	0.0036	3.0 ± 0.1
1.2	8	5.5 ± 0.3	86	7.6	1.21	0.0036	3.7 ± 0.1
1.3	8	9.0 ± 0.5	86	7.6	1.21	0.0036	10.0 ± 0.3
1.4	8	9.7 ± 0.5	86	7.6	1.21	0.0036	13.1 ± 0.7
2.1	10	1.4 ± 0.1	86	7.6	1.39	0.0038	0.7 ± 0.1
2.2	10	2.9 ± 0.1	86	7.6	1.39	0.0038	1.8 ± 0.1
2.3	10	4.3 ± 0.2	86	7.6	1.39	0.0038	3.3 ± 0.1
2.4	10	5.9 ± 0.3	86	7.6	1.39	0.0038	5.3 ± 0.2
2.5	10	7.2 ± 0.4	86	7.6	1.39	0.0038	8.7 ± 0.2
3.1	14	1.9 ± 0.1	86	7.6	1.74	0.0043	1.1 ± 0.1
3.2	14	3.0 ± 0.1	86	7.6	1.74	0.0043	2.2 ± 0.1
3.3	14	4.2 ± 0.2	86	7.6	1.74	0.0043	4.6 ± 0.2
3.4	14	5.1 ± 0.2	86	7.6	1.74	0.0043	5.4 ± 0.2
3.5	14	3.4 ± 0.1	119	6.6	2.41	0.0051	2.6 ± 0.1
3.6	14	13.8 ± 0.6	119	6.6	2.41	0.0051	30.4 ± 1.0
3.7	14	17.4 ± 0.8	119	6.6	2.41	0.0051	41.6 ± 1.8
4.1	20	3.8 ± 0.2	119	6.6	3.10	0.0057	3.1 ± 0.1
4.2	20	9.4 ± 0.5	119	6.6	3.10	0.0057	13.1 ± 0.6
4.3	20	13.1 ± 0.6	119	6.6	3.10	0.0057	28.6 ± 1.0
4.4	20	18.5 ± 1.1	119	6.6	3.10	0.0057	38 ± 3
5.1	30	2.7 ± 0.1	119	6.6	3.85	0.0064	1.7 ± 0.1
5.2	30	6.4 ± 0.3	119	6.6	3.85	0.0064	6.1 ± 0.5
5.3	30	9.4 ± 0.5	119	6.6	3.85	0.0064	16.1 ± 0.9
5.4	30	13.9 ± 0.6	119	6.6	3.85	0.0064	21 ± 2
6.1	35	2.1 ± 0.1	119	6.6	3.94	0.0065	0.8 ± 0.1
6.2	35	4.8 ± 0.2	119	6.6	3.94	0.0065	4.4 ± 0.4
6.3	35	7.6 ± 0.4	119	6.6	3.94	0.0065	9.1 ± 0.9
6.4	35	11.4 ± 0.5	119	6.6	3.94	0.0065	13.2 ± 0.9
Rotala canopy							
7.1	20[e]	4.3 ± 0.2	447	4.7	2.82	0.0046	1.5 ± 0.1
7.2	20	8.8 ± 0.5	447	4.7	2.82	0.0046	3.9 ± 0.1
8.1	20	3.9 ± 0.2	795	3.5	5.01	0.0081	1.7 ± 0.1
8.2	20	8.4 ± 0.4	795	3.5	5.01	0.0081	6.5 ± 0.2

[a]Channel-average velocity U determined from the flow meter was equal to $\langle \overline{u} \rangle_z$ determined from the distributed velocity measurements. The uncertainty σ_U arose from small fluctuations in the pump reading. [b]d_s is the spacing between plant rows, as shown in Figure 3b. [c]Depth-average frontal area defined as $\langle a \rangle_z = mA_f/H$. [d]Channel-average *TKE*. Here, $\langle\ \rangle_Z$ denotes the horizontal- and vertical-average of distributed velocity measurements. The uncertainty is associated with the spatial variation in k_t. [e]The water depth for the *Rotala* canopy was 2 cm higher than the canopy height (18 cm). However, velocity measurements above the canopy was not possible with the Nortek Vectrino. ϕ is the fraction of canopy volume occupied by plants. The volume of the plant was measured by the Archimedes principle.

in the range 0.01 to 0.18 m/s. Since the *Rotala* canopy had a vertically uniform geometry (Figure 1), only one water depth $H = 20$ cm was considered, with two pump rates and two stem densities, producing four cases in total (Table 1).

3.3. Measurements

3.3.1. Velocity Measurements

A Nortek Vectrino measured the instantaneous velocity (u,v,w), corresponding to x (streamwise), y (lateral), and z (vertical) directions, respectively. Vertical profiles used a 1-cm vertical interval. At each point, the velocity was measured at a sampling rate of 200 Hz for 3 min. The velocity near the water surface could not be measured, since the ADV cannot sample within 5 cm below the water surface. To estimate the depth-averaged velocity, uniform velocity was assumed within this region (Maza et al., 2017). The values of signal-to-noise ratio (SNR) and correlation (CORR) were both high (i.e. SNR > 20, CORR>90%), ensuring that the measurement was reliable. Spikes in the velocity records were removed by a MATLAB code, which

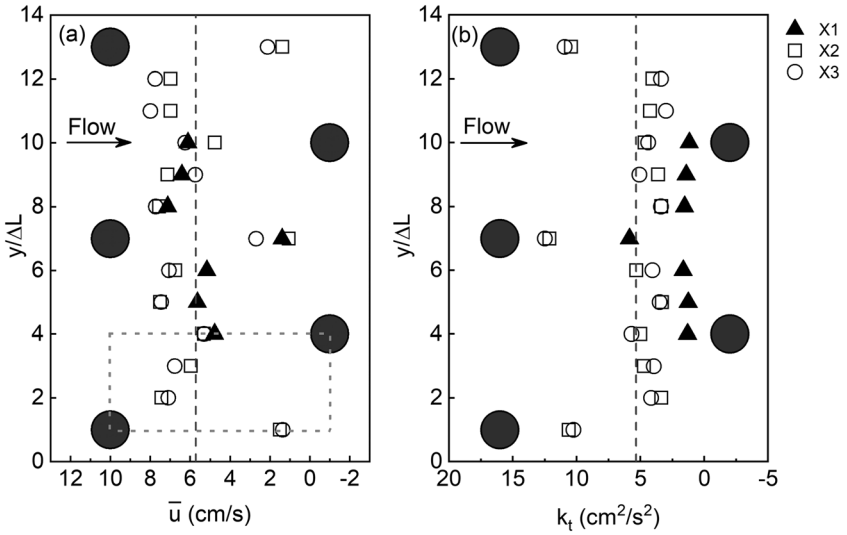

Figure 4. Lateral profiles of (a) $\overline{u}$ and (b) k_t measured midway between adjacent plant rows. The three transects are represented by different symbols: $X1$ (triangles), $X2$ (squares), and $X3$ (circles). Velocity measured at $z = 5$ cm (mid depth). Black dots indicate plant positions at the base. The horizontal dashed lines indicate the lateral average of $\overline{u}$ (subplot a) and k_t (subplot b) measured at $X2$. The red dashed box in a represents a unit cell repeated within the array that represents the velocity pattern within the array. ΔL is equal to $d_s/3$, shown in Figure 3b and Table 1.

used the acceleration threshold method described in Goring and Nikora (2002). Each velocity record was decomposed into time-averaged components ($\overline{u}$, $\overline{v}$, $\overline{w}$) and instantaneous fluctuations (u',v',w'). The turbulent kinetic energy, k_t, was defined as

$$\mathrm{k_t} = \frac{1}{2}\left(\overline{\mathrm{u'^2}} + \overline{\mathrm{v'^2}} + \overline{\mathrm{w'^2}}\right). \tag{11}$$

For both canopies of *Typha* and *Rotala*, four lateral positions (P1 to P4, Figure 3b) were chosen to capture the horizontal variation in the fully developed region of the vegetation. These points represented a unit-cell within the vegetation, which was a representative area that repeats across the array (see red dashed box in Figure 4). An initial experiment with water depth $H = 10$ cm tested the assumption that the positions P1 to P4 accurately represented the complete lateral average in the fully developed region of the vegetation. Because of the limitation of total flume length, the flow was not fully developed upstream of the vegetation. However, within the vegetation, fully developed flow was achieved by $x = X2 = 0.58$ m from the leading edge. Specifically, the velocity at $z = 5$ cm was measured across the channel width at three longitudinal positions ($X1$, $X2$, $X3$ in Figure 3b, with measurements denoted by gray squares). The lateral transects were midway between plant rows. The lateral transects of mean and turbulent velocity measured at $X2$ and $X3$ overlapped (Figure 3), which indicated that the flow was fully developed for $x \geq X2$. The same evaluation was completed for the largest flow depth ($H = 35$ cm) demonstrating fully developed flow was achieved for $x > X2$ (data not shown). In addition, the laterally averaged velocity and $\langle k_t \rangle$ within each of the four unit cells differed from the full transect (black dashed line in Figure 4) by just 1% to 2% and 1% to 7%, respectively. These data suggested that the unit cell provided a reasonable estimate for the average across the full channel width. To facilitate comparison to the force measurement (red dot in Figure 3b), the points P1 to P4 at $x = 0.65$ m (Figures 2 and 3b) were selected as the unit cell. For the *Rotala* canopy only, plants obstructed the ADV probe at some positions. To correct this, one row of plants was cleared away to create a gap of $\Delta S = 7$ cm. The analysis provided in the Supporting Information S1 indicated the effects of the gap could be neglected.

The integral length-scale, l_t, represents the scale of the dominant eddies. It can be estimated from the frequency peak $f_{p,u}$ in the frequency-weighted spectrum of $u'(t)$ (e.g., Kaimal & Finnigan, 1994, p. 34; Pearson et al., 2002, see additional details in the Supporting Information S1).

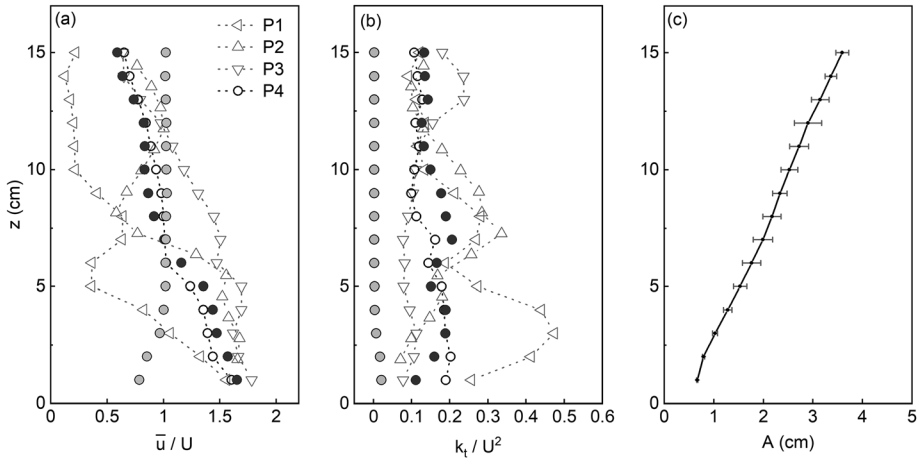

Figure 5. Vertical profiles of normalized a $\overline{u}$ and b k_t from Case 4.3 with a *Typha* canopy. Open symbols indicate profiles of (a) $\overline{u}/U$ and (b) k_t/U^2 at positions P1 to P4 defined in Figure 3b. Black solid circles indicate the lateral average of (a) $\langle\overline{u}\rangle/U$ and (b) $\langle k_t\rangle/U^2$. The velocity and k_t profiles over baseboards without vegetation are shown with gray solid circles. (c) The vertical profile of *Typha* frontal area per cm vertical interval, A [cm^2/cm]. The flow depth is H = 20 cm and the channel-average velocity is U = 13.1 cm/s.

$$l_t = \frac{|\overline{u}|}{2\pi f_{p,u}}. \tag{12}$$

3.3.2. Drag Force Measurements

Force measurements were made on an individual plant within the canopy (red dot in Figure 3b). The plant was fitted into a stainless-steel base, which was attached to a submersible 8.9 N force transducer (Futek LSB210). The force transducer was mounted into a 13-cm high hollow acrylic ramp that spanned the channel width. The ramp was 1-m long on top and 2 m at the base (Figure 2). The device was calibrated with weights of known mass, which showed a linear calibration between strain and force. For each case, the drag force was measured at a sampling rate of 1,200 Hz for 3 min. The force measured at the zero-flow condition was subtracted to account for background strain associated with the mounting position of the force transducer. Additional details are included in the Supporting Information S1.

The drag coefficient C_D for each velocity and water depth was estimated from the measured drag force, F_D, using two approaches, if the quadratic dependence of velocity on force was satisfied. Following previous studies, C_D was assumed to be constant along the vertical (e.g., Dalrymple et al., 1984; Kobayashi et al., 1993; Losada et al., 2016). The first estimate of drag coefficient, C_{D1}, was estimated from the total submerged frontal area of one plant, $A_f = \int_0^H A(z)dz$, and the channel-averaged velocity, $\langle\overline{u}\rangle_z$.

$$F_D = \frac{1}{2}\rho C_{D1} A_f \langle\overline{u}\rangle_z^{\,2}. \tag{13}$$

A second coefficient, C_{D2}, was defined from the integral of the vertically varying parameters,

$$F_D = \frac{1}{2}\rho C_{D2}\int_0^H A(z)\langle\overline{u}\rangle(z)^2 dz, \tag{14}$$

ρ is the fluid density.

4. Results and Discussion

4.1. Velocity and Turbulent Kinetic Energy

4.1.1. *Typha* Canopy

Both the individual velocity profiles within the canopy (P1 to P4 in Figure 3b) and the horizontally averaged profile within the canopy, $\langle\overline{u}\rangle$, were different from the velocity profile over bare bed, which followed a boundary layer shape (Figure 5a). In the horizontally averaged profile (black solid circles), the highest

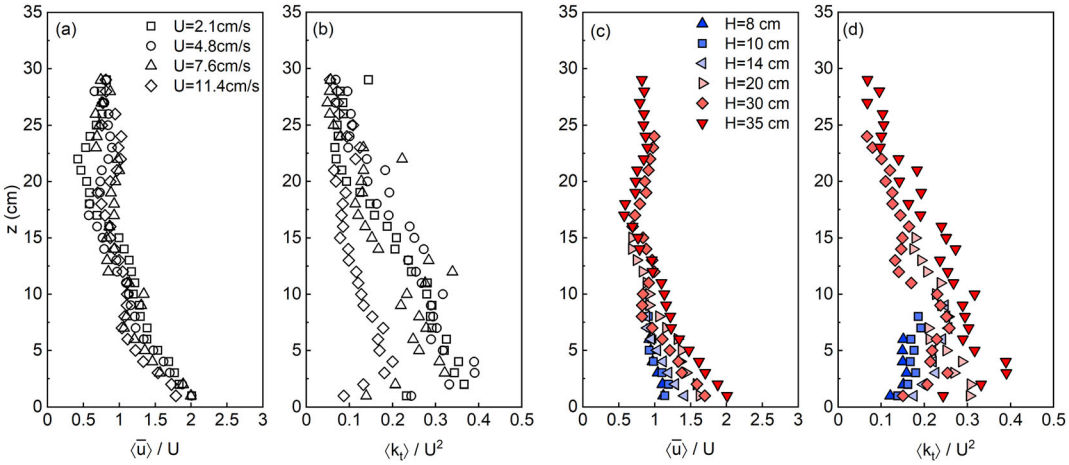

Figure 6. Vertical profiles of lateral average velocity, $\langle \overline{u} \rangle / U$, and turbulent kinetic energy $\langle k_t \rangle / U^2$, normalized by channel-average velocity for the *Typha* canopy. Subplots (a) and (b) with $H = 35$ cm and different channel-averaged velocity (legend in subplot a). Subplots (c) and (d) $U = 4.5$ cm/s for different water depths (legend in subplot c).

velocity occurred near the bed, and the velocity decreased with distance from the bed. The shape of the $\langle \overline{u} \rangle$ profile was determined by the vegetation drag, and it varied inversely with the plant frontal area (Figure 5c). Specifically, the velocity was highest where the frontal area was lowest (see also Lightbody & Nepf, 2006; Nepf, 2012). Velocity profiles at the four lateral locations varied from one another due to the proximity of individual plants. Compared with other locations, the velocity at P1 (left triangle in Figure 5a) was the lowest, consistent with this profile being directly downstream from a plant (Figure 1). It is useful to note that in almost all cases, the velocity profile at P4 (open circle in Figure 5a) was close to the lateral-average profile (black solid circles in Figure 5a), so that this position would make a useful single point measurement in canopies with staggered arrays of plants.

The turbulent kinetic energy was significantly enhanced by the canopy, relative to that measured for a base-board alone with the same velocity and water depth (Figure 5b), and measurements comparing conditions with and without the ramp confirmed that the ramp had negligible impact on k_t. For example, in Case 4.3 (Figure 5b), the channel-average turbulence intensity was $\sqrt{\langle k_t \rangle_z}/U = 0.43$ within the *Typha* canopy, which was seven times higher than the value measured for bare bed (0.07). Elevated turbulence in a canopy can be attributed to two aspects of canopy flow (King et al., 2012; Maza et al., 2017; Nepf & Vivoni, 2000). First, turbulence can be produced in the wakes of individual plant elements (the culm, stem, or leaves). Second, turbulence can be generated within the shear created from the vertical variation in plant frontal area. However, measurements discussed below indicate that shear generation was negligible.

Across different discharge rates, but with the same flow depth, the horizontally averaged velocity normalized by U collapsed to a single curve (Figure 6a). This was consistent with a velocity profile determined by the distribution of canopy drag ($C_D a$), as discussed in Lightbody and Nepf (2006). Similarly, most of the lateral-average profiles of turbulence intensity also collapsed when normalized by U^2 (Figure 6b), with the only exception being for the highest velocity, which exhibited a proportionally lower magnitude of turbulence intensity.

The normalized profiles of velocity and $\langle k_t \rangle$ had some variation with water depth (Figures 6c and 6d). Specifically, as water depth increased (blue to red symbol color), the normalized velocity near the bed increased. This was associated with the vertical variation in frontal area (Figure 1). As the water depth increased, there was a greater difference in frontal area between the water surface and the bed, which diverted more of the flow toward the bed, where the frontal area was lower. Further, as the velocity near the bed increased, relative to the channel average ($\langle \overline{u} \rangle / U > 1$), the normalized $\langle k_t \rangle$ near the bed also increased. This was consistent with turbulence generation dominated by local wake production, that is, $\langle k_t \rangle \sim \langle \overline{u} \rangle^2$, such that $\langle k_t \rangle / U^2$ increased as $\langle \overline{u} \rangle / U$ increased.

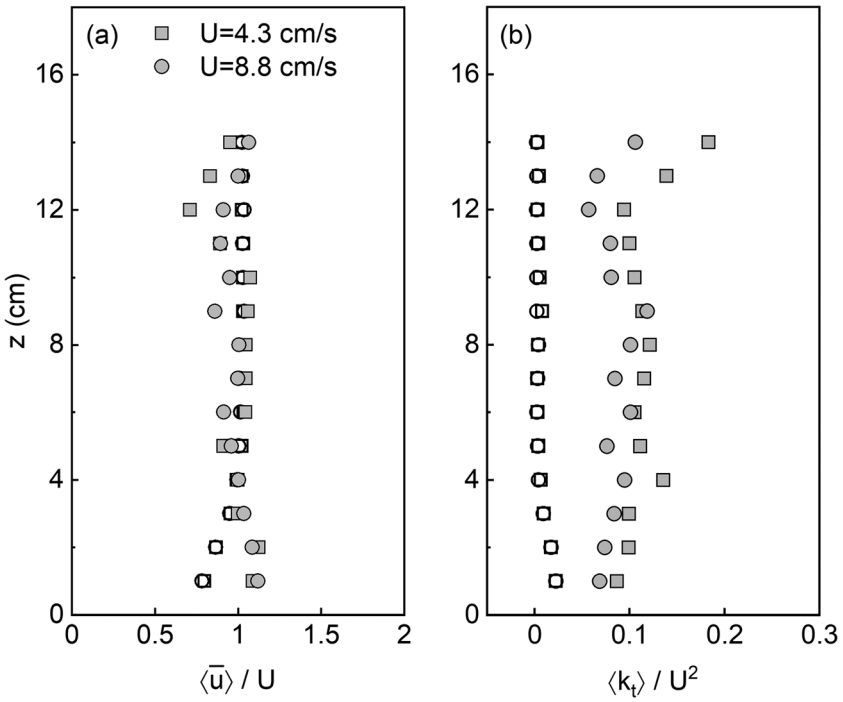

Figure 7. Vertical profiles of (a) laterally averaged velocity, $\langle \bar{u} \rangle / U$, and (b) turbulent kinetic energy $\langle k_t \rangle / U^2$, normalized by channel-average velocity for the *Rotala* canopy with $\phi = 0.0081$. Open symbols represent the bare bed.

This study considered an array of closely spaced plants, such that flow was deflected toward the bed, where the array frontal area was smallest. In contrast, when the plants are spaced far apart, which can be explored by considering a single plant, lateral flow deflection is also possible, which impacts the velocity and turbulence in the wake of single plant. Specifically, turbulence has been observed to be higher in the wake of a tree crown than its trunk, because lateral flow deflection around the crown produced strong shear layers in the wake of an isolated tree (Fig. 11 in Boothroyd et al., 2017; Kitsikoudis et al., 2016; Yagci et al., 2010).

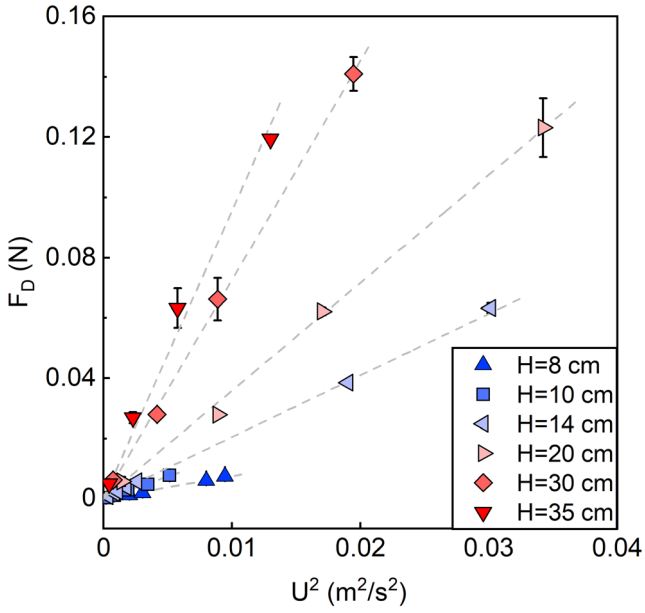

Figure 8. Measured drag force as a function of U^2. Symbol color corresponds to flow depth. The vertical error bars reflect replicate measurements of drag force. Gray dashed lines indicate the linear fit curves with zero intercept.

The vertical profile of turbulence intensity also had some dependence on water depth. For smaller water depth ($H \leq 10$ cm, blue symbols in Figure 6d), the turbulence intensity was fairly uniform over the vertical profile. For larger depths (red symbols in Figure 6d), the vertical distribution of turbulence intensity was more complicated. Moving away from the bed, $\langle k_t \rangle / U^2$ initially increased (up to $z \approx 5$ cm), then decreased, then reached an almost uniform value above $z > 20$ cm. The vertical variation in turbulence intensity was associated with vertical variation in plant morphology and specifically with vertical variation in both canopy frontal area (a) and integral length-scale (l_t), as discussed in section 4.3.

4.1.2. *Rotala* Canopy

The second plant, *Rotala*, was selected for its vertically uniform distribution of frontal area, which contrasted with the nonuniform *Typha*. Consistent with this, the lateral average velocity and $\langle k_t \rangle$ profiles within a canopy of *Rotala* were more vertically uniform (solid symbols in Figure 7) than those measured in the *Typha* (Figure 6).

4.2. Forces Exerted on One Plant Within the Canopy

Drag forces were measured on the plant located downstream of P4 (red dot in Figure 3b). For all flow depths, the drag force increased linearly

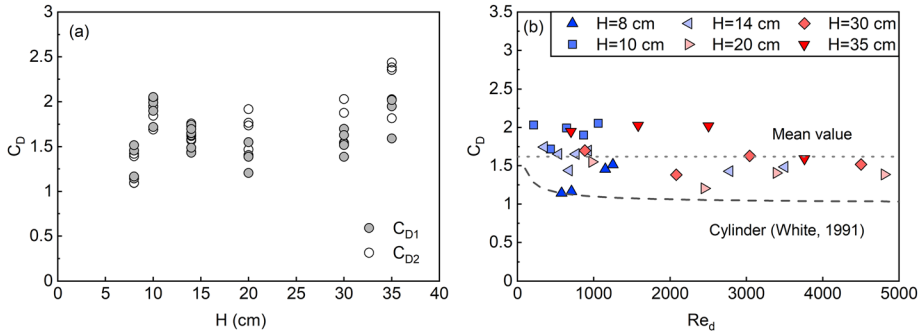

Figure 9. (a) Drag coefficients estimated for *Typha* using two methods, C_{D1} and C_{D2}, estimated from Equations 13 and 14, are represented by solid and open marks, respectively. The uncertainty in C_D was within 0.11, arising from the uncertainty of frontal area. (b) C_{D1} estimated from Equation 13. No significant relationship was observed between drag coefficient C_{D1} and plant Reynolds number $Re_d = Ud_e/\nu$, in which $d_e = A_f/H$. The gray dotted line indicates the mean value across all *Typha* measurements. Empirical relation for a smooth, isolated cylinder of diameter d shown with dashed line, ($C_D = 1 + 10Re_d^{-2/3}$ in White, 1991, $Re_d = Ud/\nu$).

with the square of the velocity (Figure 8), indicating that a quadratic drag law was appropriate. This was consistent with the observation that the plants did not reconfigure (bend) significantly in response to the flow, as reconfiguration has been previously shown to manifest in drag dependence with velocity that is weaker than quadratic (e.g., Albayrak et al., 2014; Fathi-Maghadam & Kouwen, 1997; Luhar & Nepf, 2011; Sand-Jensen, 2003).

The drag coefficient can be defined with the channel-average velocity and total submerged plant area (C_{D1}, Equation 13), or by a piecewise integration of the velocity and frontal area profile (C_{D2}, Equation 14). The two methods produced similar values (Figure 9a), with a percentage difference between C_{D1} and C_{D2} of 2.3% to 15.5%. This demonstrated that the simpler Equation 13 can be a good estimator in the field. Further, the drag coefficient showed little variation with water depth (Figure 9a), even as the frontal area per volume a changed with depth (Figure 1).

The drag coefficient had no clear dependence on Reynolds number $Re_{\mathrm{d}} = Ud_e/\nu$ (Figure 9b), defined using the equivalent diameter, d_e, which is the diameter of an emergent cylinder with the same submerged frontal area, A_f, in water depth H,

$$\mathrm{d_e} = \frac{\mathrm{A_f}}{\mathrm{H}}. \tag{15}$$

The average drag coefficient for *Typha* across all conditions was $C_D = 1.62 \pm 0.10$ (SE), and this value was used in all subsequent analyses. The *Rotala* showed similar behavior, in that C_D was not a function of velocity or water depth, and the average value was $C_D = 1.75 \pm 0.15$ (SE). These values fall in the upper range of drag coefficients observed for cylinders within an array (C_D = 1 to 2, for $Re_d \geq 600$; Fig. 5 in Cheng & Nguyen, 2011), which is greater than the value for an isolated cylinder (dashed line in Figure 9b). For the plants considered here, a higher value of C_D might be attributed to the greater wetted perimeter, compared to a rigid cylinder.

4.3. Modified Turbulent Kinetic Energy Model

4.3.1. Shear Production and Wake Production

Recall that Tanino's model for canopy turbulence (Tanino & Nepf, 2008) was based on an array of vertical, circular cylinders, for which vertical shear, and thus shear production, was negligible. For a *Typha* canopy, vertical variation in frontal area produced vertical shear in the velocity profile (Figure 6), such that shear-production may be important in the turbulent kinetic energy budget. However, for the emergent *Typha* canopy, the measured shear-production term (Equation 5) was negligible compared to the wake-production term (Equation 6, Figure 10). Tinoco (2011) similarly concluded that shear-production was negligible compared to wake production within an emergent canopy of *Watermilfoil* (see Figs. 2.5 and 5.25 in Tinoco, 2011).

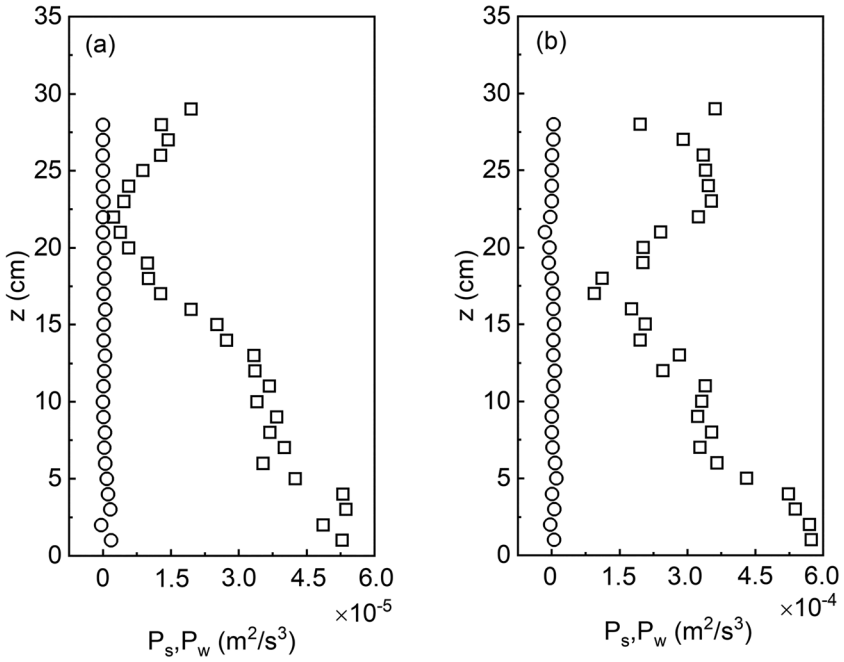

Figure 10. Shear production P_s (circles) estimated from Equation 5 and wake production P_w (squares) estimated from Equation 6 for the largest water depth ($H = 35$ cm) within the *Typha* canopy, which exhibited the greatest shear in the velocity profile. (a) Case 6.1: $U = 2.1$ cm/s. (B) Case 6.2: $U = 4.8$ cm/s.

4.3.2. Integral Length-Scale

Within the *Typha* canopy, the laterally averaged integral length-scale varied with distance from the bed (Figure 11b), reflecting the *Typha* morphology. Specifically, near the bed the leaves were bundled together, forming a solid, cylindrical culm, but farther from the bed ($z > 10$ cm) the leaves spread out enough to allow flow to pass in between the leaves (Figure 1). Consistent with this, near the bed ($z < 10$ cm), the integral length scale had an approximately constant value, 1.5 ± 0.3 cm (SE), which corresponded to the culm diameter ($d_c = 1$ to 2 cm, Figure 1). In the upper region of the canopy, $z > 17$ cm, the integral scale was also a constant, but with a smaller value, 0.2 ± 0.1 cm (SE), which corresponded to the width of the leaves (0.1 to 0.4 cm). In between these two regions, the integral length-scale varied smoothly between the culm scale and the leaf scale.

The channel-average integral length-scale, $\langle l_t \rangle_z$, as a function of water depth is shown in Figure 12. It was approximately constant for small depth ($H \leq 14$ cm) but decreased with increasing depth for $H > 14$ cm. The depth-dependent variation in $\langle l_t \rangle_z$ arose from the change in plant morphology with distance from the bed (Figure 1). For shallow depth (H<14 cm), only the base of the plant was submerged, a region in which the leaves were just emerging from the culm and appeared like a solid object (Figure 1a). As the water depth increased above 14 cm, the submerged part of the plant included the region with spread leaves (Figure 1a), and flow passing in between individual leaves resulted in turbulence at the leaf-scale (0.1 to 0.4 cm). As a result, the integral length scale decreased for water depths above 14 cm (Figure 11). Based on the above description, a simple model was proposed

$$l_t = \begin{cases} d_e = 1.5, & z < 10 \\ 3.6 - 0.19z, & 10 \leq z < 17, \ (\text{cm}) \\ w_1 = 0.2 & z \geq 17 \end{cases}. \tag{16}$$

Equation 16 is compared with measured values in Figure 12 (dashed line). Note that the equivalent diameter d_e was also a function of water depth (Equation 15). For small depth ($H \leq 10$ cm), the equivalent diameter was close to l_t (Figure 12). However, significant deviation between d_e and l_t was observed for water depth above 14 cm, when the individual leaf scale became important.

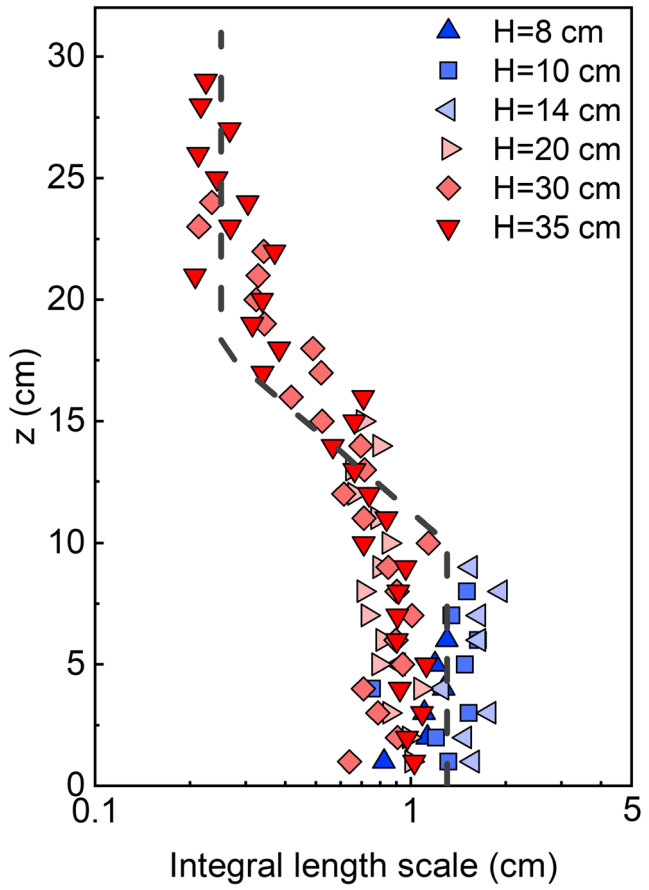

Figure 11. Vertical profiles of lateral average integral length-scale for different depths (indicated by color) in the *Typha* canopy. Dashed line segments indicate the length-scale values used in the turbulence model, based on the averages across all 28 *Typha* cases (Table 1). Shown here: Case 1.1: $H = 8$ cm, $U = 4.5$ cm/s; Case 2.3: $H = 10$ cm, $U = 4.3$ cm/s; Case 3.5: $H = 14$ cm, $U = 3.4$ cm/s; Case 4.1: $H = 20$ cm, $U = 3.8$ cm/s; Case 5.2: $H = 30$ cm, $U = 6.4$ cm/s; Case 6.2: $H = 35$ cm, $U = 4.8$ cm/s.

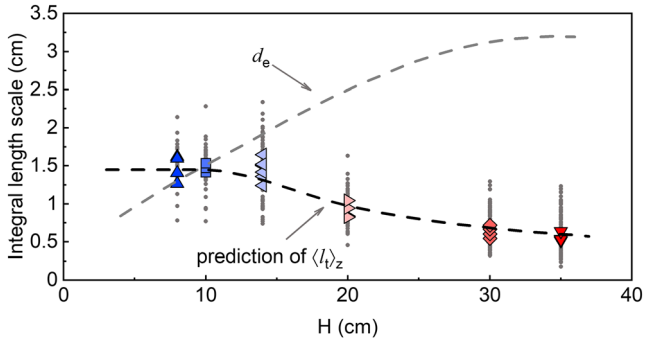

Figure 12. The channel average integral length-scale $\langle l_t \rangle_z$ versus water depth H for the *Typha* canopy. Small gray dots indicate lateral-average length-scale $\langle l_t \rangle$.The black dashed line is depth-average of Equation 16. The gray dashed line is the equivalent diameter d_e (Equation 15). Symbol color given in Figure 11.

The integral length-scales measured in the *Rotala* canopy were more uniform (Figure 13a), compared to the *Typha* canopy (Figure 11b), reflecting *Rotala*'s more vertically uniform morphology. Further, for the *Rotala*, the equivalent diameter $d_e = 0.68 \pm 0.13$ cm (SE) defined by Equation 15 was not a function of flow depth and provided a good prediction of the integral length scale (dashed line in Figure 13b). This suggested that, for plants with vertically uniform frontal area, the integral length scale can be estimated from the equivalent diameter d_e, if the mean spacing between stems is larger than d_e, based on similarity with a cylinder array (Tanino & Nepf, 2008).

4.3.3. The *TKE* Model for *Typha*

The vertical distribution of laterally averaged *TKE*, $\langle k_t \rangle(z)$, within the *Typha* canopy was predicted by assuming that Equation 10 held at every vertical position. Specifically,

$$\langle k_t \rangle(z) = \gamma^2 \left(C_D \frac{a(z)\langle l_t \rangle(z)}{2(1-\phi(z))} \right)^{2/3} [\langle \overline{u} \rangle(z)]^2 \tag{17}$$

with the integral length-scale defined by Equation 16. Note that the form drag coefficient in Equation 10 was replaced by the measured value, $C_D = 1.62 \pm 0.11$ (SE), as described in section 4.2. This was reasonable, because Etminan et al. (2017) showed that $C_D^{form} \approx 0.9\, C_D$, and this difference was not considered significant relative to other uncertainties in the parameter estimation. The scale coefficient, $\gamma^2 = 1.6 \pm 0.4$ (SE), was determined with a linear fit between measured $\langle k_t \rangle$ and $[C_D a \langle l_t \rangle / 2(1-\phi)]^{2/3} \langle \overline{u} \rangle^2$, assuming an intercept of zero (Figure 14a). Although the error ranges overlapped, the mean value of γ^2 was larger than the value determined for an array of rigid cylinders (γ^2=1.1 ± 0.2, Eq. 3.33 in Tanino, 2008), suggesting that γ^2 may be sensitive to the plant morphology.

The predicted and measured $\langle k_t \rangle$ for the largest water depth (which had the greatest vertical variation in morphology and velocity) are compared in Figure 14b. The prediction (red symbols) exhibited vertical variation consistent with the measurement (gray symbols), supporting the idea that Equation 17 can represent the vertical variation in the canopy turbulence. Note that Equation 17 overpredicted $\langle k_t \rangle$ near the bed. This was most likely due to the assumption that the near-bed integral length-scale was equal to the average across all depth cases (1.5 cm, see Equation 16), which was larger than the measured integral length-scale for this water depth (compare red triangles, $H = 35$ cm, to the dashed line shown in Figure 11). Further, the model neglected the shear-production associated with bed-shear. However, the comparison between $\langle k_t \rangle$ measured for bare-bed and with a *Typha* canopy (Figure 5) suggested that bed-generated turbulence made a very small contribution (~16%) to the total turbulence, so it was reasonable to neglect it.

The channel-average turbulent kinetic energy, $\langle k_t \rangle_z$, can be estimated by integrating Equation 17 over depth. Alternatively, for practical purposes, it is useful to consider whether the channel-average turbulent kinetic energy can be predicted using just channel-averaged parameters, each denoted by $\langle\ \rangle_z$, that is,

$$\langle k_t \rangle_z = \gamma^2 \left(C_D \frac{\langle a \rangle_z \langle l_t \rangle_z}{2(1-\langle \phi \rangle_z)} \right)^{2/3} U^2, \tag{18}$$

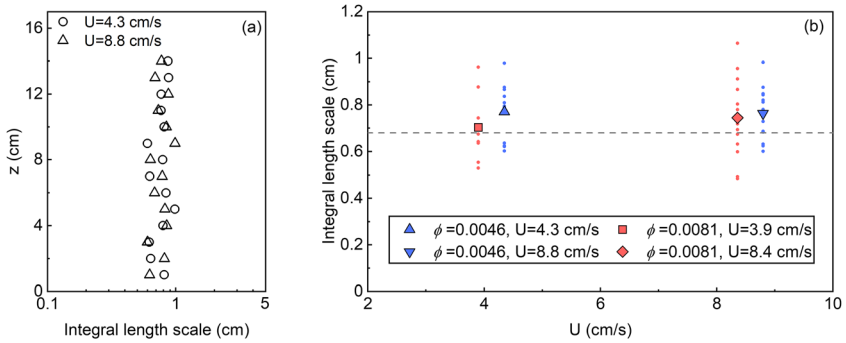

Figure 13. (a) Vertical profiles of the laterally averaged integral length-scale $\langle l_t \rangle$ for *Rotala* with $\phi = 0.0046$. (b) The channel-average integral length-scale for the *Rotala* for all cases in Table 1. The low $\phi = 0.0046$ and high $\phi = 0.0081$ are represented by blue and red colors, respectively. Dots indicate lateral-average $\langle l_t \rangle$ at each vertical position within the canopy. Symbols represent the channel-average integral length scale, $\langle l_t \rangle_z$.

with $C_D = 1.62 \pm 0.11$. $\langle a \rangle_z$ is the depth-average of $a(z)$ (Table 1), and $\langle l_t \rangle_z$ is the depth-average of Equation 16. Remember that the depth-average is taken only over the submerged depth. The canopy-average estimated from the depth-average of Equation 17 and from Equation 18 are compared to the measured values in Figure 15. The fitted constant $\gamma^2 = 1.6 \pm 0.3$ and 1.6 ± 0.4 (SE) for Equations 17 and 18, respectively, are the same. Therefore, the simpler Equation 18 can be reliably used to predict the channel-average turbulent kinetic energy. Finally, in both Equations 17 and 18, we assumed $C_D = 1.62$. In fact, the value of C_D differed somewhat between cases, with a range 1.14 to 2.05 (Figure 9). To consider the impact of this variation, the measured $\langle k_t \rangle_z$ was fit to $[C_D \langle a \rangle_Z \langle l_t \rangle_z / 2(1 - \langle \phi \rangle_z)]^{2/3} U^2$ using the specific C_D of each case. The resulting scale constant $\gamma^2 = 1.7 \pm 0.3$ was the same within uncertainty to the fit with constant C_D, indicating that this assumption was reasonable.

4.3.4. Sensitivity of Model Parameters

The channel-average *TKE* model (Equation 18) includes six parameters. The frontal area and solid volume fraction can be estimated from plant morphology, and the canopy-averaged velocity can be estimated from measured discharged. However, there is less confidence in the scaling constant, γ, drag coefficient, C_D, and integral length-scale $\langle l_t \rangle_z$. Therefore, it is useful to understand the sensitivity of the prediction to the choice of these parameters. From previous studies (Etminan et al., 2017; King et al., 2012; Maza et al., 2017; Tanino & Nepf, 2008; Zhang et al., 2018), the values of γ^2 and C_D were expected to be order one, so we considered the range 0.5 and 2.5. The value of l_t was chosen to vary over the range 0.1 and 3.0 cm to capture the range of leaf

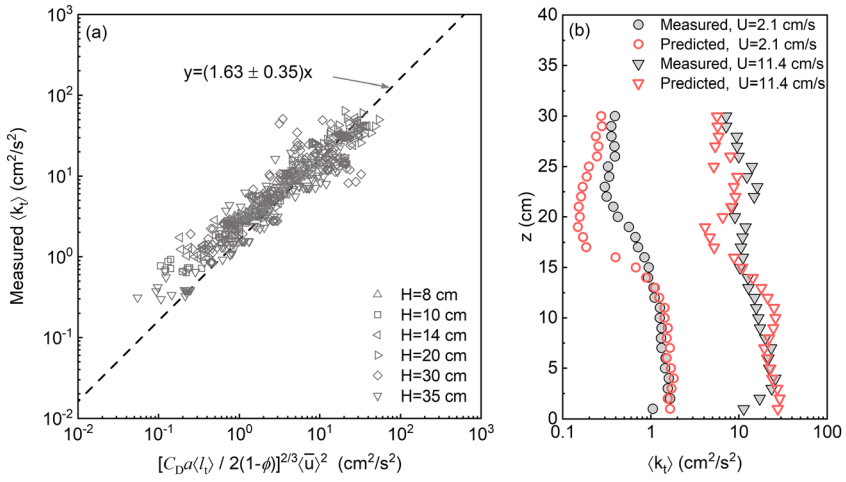

Figure 14. (a) Measured $\langle k_t \rangle$ versus $[C_D a \langle l_t \rangle / 2(1 - \phi)]^{2/3} \langle \overline{u} \rangle^2$, from Equation 17. The linear best fit (dashed line) indicated $\gamma^2 = 1.6 \pm 0.4$. (b) Comparison of measured and predicted $\langle k_t \rangle$ for Case 6.1 and 6.6 with $H = 35$ cm.

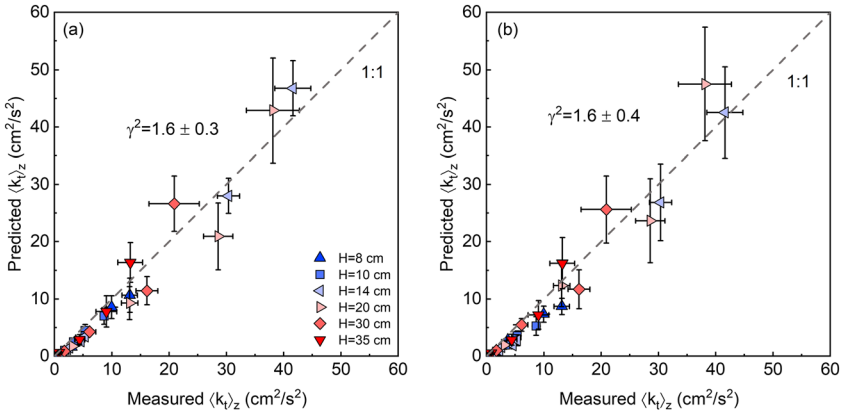

Figure 15. Comparison of predicted and measured channel-average $\langle k_t \rangle_z$, using (a) depth-average of Equation 17 with $\gamma^2 = 1.6 \pm 0.3$ and (b) Equation 18 with $\gamma^2 = 1.6 \pm 0.4$. The horizontal error bars arise from the spatial variation of measured $\langle k_t \rangle_z$ (SE). The vertical error bars are associated with the uncertainty of velocity and γ^2.

width to equivalent diameter d_e. The deviation between predicted, $\langle k_{t,p} \rangle_z$, and measured, $\langle k_{t,m} \rangle_z$, turbulent kinetic energy was evaluated using the root-mean-square deviation, $RMSD = \sqrt{\sum \left(\langle k_{t,m} \rangle_z - \langle k_{t,p} \rangle_z \right)^2 / N}$, with N the total number of cases. To facilitate comparison, the $RMSD$ was normalized by the average $\langle k_{t,m} \rangle_z$. This ratio, $RMSD/\langle k_{t,m} \rangle_z$, represents a percentage error (Figure 16).

Consistent with Figure 15, $\gamma^2 = 1.6$ resulted in the minimum percentage error (Figure 16a). For the drag coefficient, the minimum error was associated with $C_D = 1.37$, which was smaller than the mean measured drag coefficient (1.62). However, the percentage error changed by only 2% between $C_D = 1.37$ and $C_D = 1.62$, indicating a relatively low sensitivity to C_D. As a reference point, an acceptable prediction was defined by a 40% error (red dashed line in Figure 16), based on the uncertainty in fitted $\gamma^2 = 1.6 \pm 0.3$. Based on this, C_D values between 1.0 and 1.8 provided reasonable estimates (i.e., 40% uncertainty). It is of practical interest to note that even the simple assumption of $C_D = 1$ and $\gamma^2 = 1$ yielded just 60% error.

The most difficult parameter to define is the channel-average integral length-scale $\langle l_t \rangle_z$. Drawing on a similarity to an array of cylinders, one might suggest $\langle l_t \rangle_z = d_e$, defined by Equation 15. Because d_e is a function of water depth (Figure 12), we considered two depths, $H = 10$ cm and 35 cm, for which $d_e = 1.5$ cm and 3.0 cm, respectively (Figure 16c). For $H = 10$ cm (solid line), the minimum error was associated with $\langle l_t \rangle_z = 1.5$ cm, in agreement with both the measured $\langle l_t \rangle_z$ (Figure 12) and also with d_e. This is consistent with the near-bed morphology of *Typha*, with the leaves bundled into a nearly cylindrical culm of diameter 1 to 2 cm (Figure 1). In contrast, for $H = 35$ cm (dashed line), the minimum error was associated with $\langle l_t \rangle_z = 0.6$ cm, consistent with the measured $\langle l_t \rangle_z$ (Figure 12) but significantly smaller than $d_e = 3.0$ cm. This was due to the fact that,

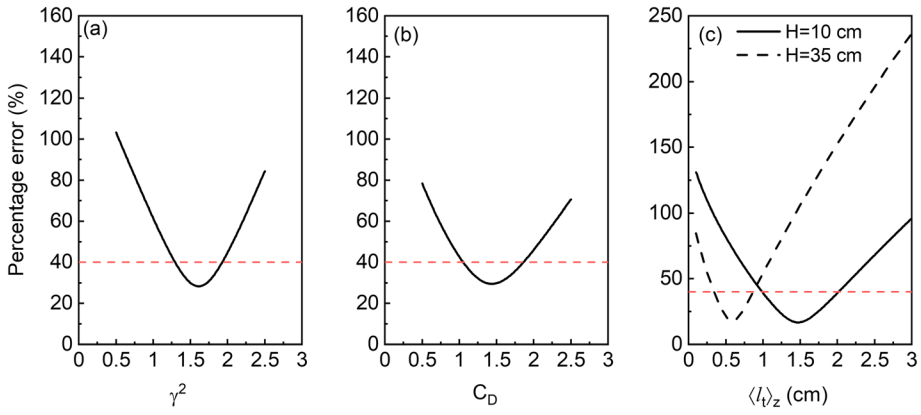

Figure 16. Percentage error between predicted (Equation 18) and measured $\langle k_t \rangle_z$, with variation in parameters (a) γ^2, (b) C_D, and (c) $\langle l_t \rangle_z$. In each subplot, one parameter is varied, with all others s held constant at measured or best-fit values.

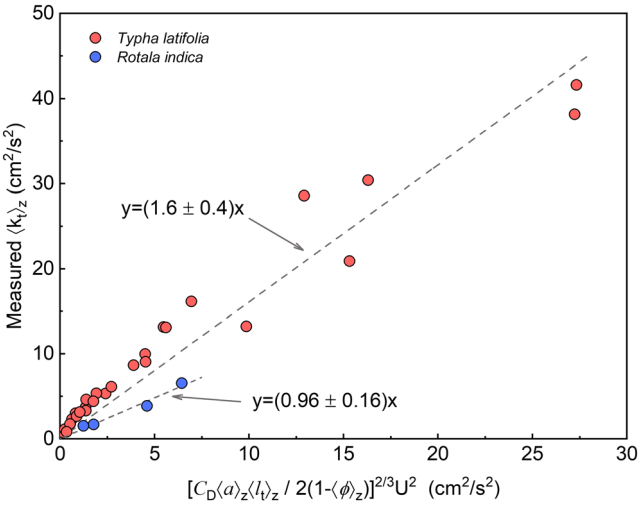

Figure 17. Measured channel-average $\langle k_t \rangle_z$ versus $[C_D \langle a \rangle_z \langle l_t \rangle_z / 2(1 - \langle \phi \rangle_z)]^{2/3} U^2$, which is the right-hand side of Equation 18, excluding γ^2. Based on a linear fit, $\gamma^2 = 0.96 \pm 0.16$ for *Rotala* (blue dots) and $\gamma^2 = 1.6 \pm 0.4$ for *Typha* (red dots). Gray dashed lines represent the linear fit of each data set.

for $z > 14$ cm, the *Typha* leaves are separated (Figure 1a), allowing flow in between individual leaves, resulting in turbulence at the leaf-scale (0.1 to 0.4 cm), which depressed the channel average value of $\langle l_t \rangle_z$ (Figure 12). This comparison suggested that for plants with leaves bundled at the base, one should not generally assume $\langle l_t \rangle_z = d_e$.

4.3.5. The *TKE* Model for *Rotala*

In comparison to the *Typha* canopy, with leaves bundled at the base, the *Rotala* canopy had leaves distributed over the length the stem, making the plant vertically more uniform (Figure 1). The vertically distributed leaves resulted in $\langle l_t \rangle_z = d_e$ at all distances from the bed (Figure 13), suggesting that, unlike *Typha*, $\langle l_t \rangle_z$ was not a function of water depth. Using the measured $\langle l_t \rangle_z = 0.68$ cm (Figure 12) and $C_D = 1.75 \pm 0.15$ (SE), the measured $\langle k_t \rangle_z$ was compared to $[C_D \langle a \rangle_Z \langle l_t \rangle_z / 2(1 - \langle \phi \rangle_z)]^{2/3} U^2$ (Figure 17). The best-fit slope indicated $\gamma^2 = 0.96 \pm 0.16$ (SE). This value was the same, within uncertainty, as that determined for an array of circular cylinders ($\gamma^2 = 1.1 \pm 0.2$ in Tanino, 2008).

The fitted value of γ^2 was larger for the *Typha* canopy than for the *Rotala* canopy. Recall that, even though vertical shear was created by the vertical variation in the *Typha* morphology, the measured shear production was negligible, compared to the wake production (Figure 10). Therefore, this difference cannot be attributed to shear production. However, the vertical variation in *Typha* morphology was also associated with a vertical variation in integral length-scale (Figure 11), which may not be well represented by a geometric average over the canopy height.

4.4. Prediction of Velocity Profile Within *Typha* Canopy

For a *Typha* canopy, the frontal area per canopy volume, a, is a function of distance above the bed, and this creates a velocity profile in which the velocity varied inversely with a. The viscous and Reynolds stresses were much smaller than the canopy drag (data not shown), such that fully developed flow through the emergent canopy can be described as in Lightbody and Nepf (2006).

$$0 = \underbrace{-g\frac{\partial \eta}{\partial x}}_{\substack{\text{pressure} \\ \text{foring term}}} \underbrace{-\frac{1}{2}\frac{C_D a}{(1-\phi)}\langle \overline{u} \rangle^2}_{\substack{\text{vegetatation} \\ \text{drag}}}. \tag{19}$$

The hydrostatic pressure gradient is associated with the water surface slope $\partial\eta/\partial x$, and the vegetation drag is represented by a distributed, quadratic drag force, as in Equation 13. Since $\partial\eta/\partial x$ is not a function of distance from the bed, the quantity $C_D a \langle \overline{u} \rangle^2$ must also be a constant over depth. Therefore, the velocity varies inversely with canopy morphology; specifically, $\langle \overline{u} \rangle(z) \propto 1/\sqrt{C_D a(z)}$.

Recall that the drag coefficients estimated from Equations 13 and 14 were similar (Figure 9a), such that we can equated the two definitions of the drag coefficient,

$$\frac{2F_D}{\rho A_f \langle \overline{u} \rangle_z^2} = \frac{2F_D}{\rho \int_0^H A \langle \overline{u} \rangle^2 dz}. \tag{20}$$

Recall that $\langle a \rangle_z = mA_f/H$, $a(z) = mA(z)$, and $\langle \overline{u} \rangle_z = U$. Combining Equations 19 and 20,

$$\frac{\langle \overline{u} \rangle(z)}{U} = \sqrt{\frac{\langle a \rangle_z}{a(z)}}. \tag{21}$$

Equation 21 provides a way to predict the profile $\langle \overline{u} \rangle(z)$ within an emergent canopy from the profile of canopy frontal area, $a(z)$, and the channel discharge, U. This would be useful in the field, sampling the

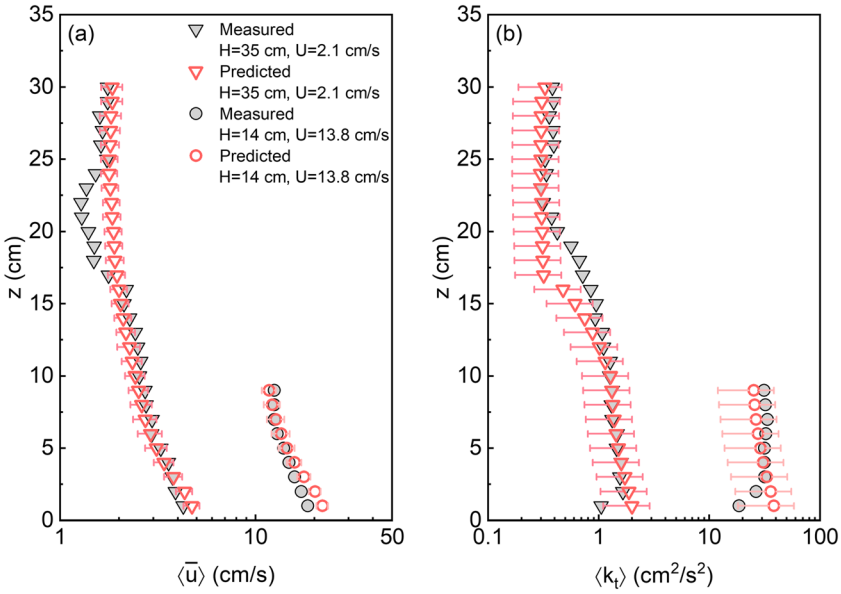

Figure 18. Comparison of measured (gray symbols) and predicted (red symbols) $\langle \overline{u} \rangle$ (subplot a) and $\langle k_t \rangle$ (subplot b) in a *Typha* canopy for water depths $H = 14$ cm (circles) and 35 cm (triangles). Velocity predicted from Equation 21 and $\langle k_t \rangle$ predicted from Equations 16, 17, and 21. The horizontal error bars arise from the uncertainty in U (Table 1), frontal area (Figure 1), and $\gamma^2 = 1.6 \pm 0.4$ (SE). Velocity was not measured within 5 cm of the water surface.

plant morphology once and then predicting the velocity profile from the channel average velocity. Combining Equations 16, 17, and 21, the $\langle k_t \rangle$ profile can also be predicted from $a(z)$ and U. Predictions of velocity based on Equation 21 and of $\langle k_t \rangle$ based on Equations 16, 17, and 21 had good agreement with the measured values (Figure 18). Small deviations between predicted and measured velocity existed near the bed, because the velocity prediction did not account for the bed drag. A more significant difference between predicted and measured velocity occurred in the upper canopy for $H = 35$ cm, which might be attributed to local variations in leaf structure that were not adequately represented by the laterally averaged frontal area. The values of $\langle k_t \rangle$ were overpredicted very close to the bed, which was attributed to two factors. First, for the larger water depth ($H = 35$ cm in Figure 18), the near-bed integral length-scale was over-predicted by the simplified Equation 16, as illustrated in Figure 11. Second, for the smaller water depth ($H = 14$ cm in Figure 18), the overestimation of near-bed velocity contributed to an overestimation of near-bed $\langle k_t \rangle$.

4.5. Field Application

For the flow and depth conditions considered in this study, the flexible plants did not reconfigure. Because reconfiguration can alter the plant drag and thus the turbulence generation, the proposed turbulence should only be applied for conditions with limited reconfiguration. To understand this constraint, here, we describe a method to estimate the flow conditions that would generate reconfiguration. For emergent plants, the buoyancy of the plant material is generally not a significant restoring force, so that the tendency to reconfigure can be described by the Cauchy number (Luhar & Nepf, 2011). The Cauchy number, C_a, describes the relative magnitude of hydrodynamic drag and the restoring force due to plant rigidity.

$$C_a = \frac{1}{2}\frac{\rho C_D b U^2 l^3}{EI}, \tag{22}$$

in which E is the elastic modulus and I is the second moment of area. For a flat leaf, $I = bt^3/12$, with b, t, and l defining the lead width, thickness, and length, respectively. When $C_a \leq 1$, the plant rigidity is sufficient to resist bending, and the plant matches the conditions considered in this study. The velocity at which reconfiguration begins can be estimated from Equation 22. We consider an example for *Typha*. Since leaves are more flexible than a stem, the leaves set the constraint for when reconfiguration

begins. Liu et al. (2017) measured the rigidity of *Typha* leaves using a three-point bending test. From Tab. 1 and Fig. 4 in Liu et al. (2017), an average leaf rigidity was inferred to be $EI = 8.5 \pm 1.2 \times 10^{-4}$ Pa·m^4 (SE). The leaf length $l = 24$ cm, and width $b = 1.5$ cm. Assume $C_D = 1$ and that the leaf is fully submerged, then $C_a > 1$ corresponds to $U > 10$ cm/s. This means that a quadratic drag law would be expected up to $U = 10$ cm/s in the field, and the proposed turbulence model could be applied directly within this velocity range. The velocity range 0 to 10 cm/s is representative of values measured in natural marshes (e.g., Fig. 1 in Leonard & Luther, 1995, and Fig. 4 in Leonard & Croft, 2006), indicating that the drag and turbulence models describe in this paper could be applied to many natural settings. Importantly, if the leaf is emergent, then the hydrodynamic drag only acts on the submerged portion, and water depth H replaces leaf length, l, in Equation 22. For example, for $H = 20$ cm, the velocity needed for the onset of reconfiguration increases to 13 cm/s.

5. Conclusion

Velocity and forces on individual plants were measured within canopies of *Typha* and *Rotala*. Within the canopies, the turbulent kinetic energy was significantly enhanced, relative to flow in a bare channel with the same channel-average velocity. For the *Typha* canopy, which had a nonuniform vertical distribution of frontal area, the flow parameters were also nonuniform, with smaller velocity, integral length-scale, and *TKE* in the canopy region with higher frontal area. For the *Rotala* canopy, which had a uniform vertical distribution of frontal area, the velocity, integral length-scale and *TKE* were also vertically uniform. A model for the channel-average *TKE* (Equation 18) was shown to provide a good prediction for both canopies. For canopies with vertically uniform morphology, like *Rotala*, the integral length scale $\langle l_t \rangle_z$ can be estimated as the equivalent diameter $d_e = A_f/H$. For nonuniform canopies, such as *Typha*, $\langle l_t \rangle_z$ varies with depth (e.g., Equation 16).

Acknowledgments
This study received support from the NSF Grant EAR 1854564 and NAS Gulf Research Program. Any opinions, findings, and conclusions in this paper are those of the author(s) and do not necessarily reflect the views of the funding agencies. Yuan Xu was supported by the China Scholarship Council and the National Natural Science Foundation of China (51879138). The authors thank Tian Zhao for his assistance with the experiments and Danxun Li for his insightful discussions. The data used to generate key figures in this paper are available through Figshare at this site (https://doi.org/10.6084/m9.figshare.12228812.v2).

References

Albayrak, I., Nikora, V., Miler, O., & O'Hare, M. T. (2014). Flow–plant interactions at leaf, stem and shoot scales: Drag, turbulence, and biomechanics. *Aquatic Sciences*, *76*(2), 269–294. https://doi.org/10.1007/s00027-013-0335-2

Barbier, E. B., Hacker, S. D., Kennedy, C., Koch, E. W., Stier, A. C., & Silliman, B. R. (2011). The value of estuarine and coastal ecosystem services. *Ecological Monographs*, *81*(2), 169–193. https://doi.org/10.1890/10-1510.1

Bennett, S. J., Wu, W., Alonso, C. V., & Wang, S. S. Y. (2008). Modeling fluvial response to in-stream woody vegetation: Implications for stream corridor restoration. *Earth Surface Processes and Landforms*, *33*(6), 890–909. https://doi.org/10.1002/esp.1581

Boothroyd, R. J., Hardy, R. J., Warburton, J., & Marjoribanks, T. I. (2017). Modeling complex flow structures and drag around a submerged plant of varied posture. *Water Resources Research*, *53*, 2877–2901. https://doi.org/10.1002/2016WR020186

Cheng, N.-S., & Nguyen, H. T. (2011). Hydraulic radius for evaluating resistance induced by simulated emergent vegetation in open-channel flows. *Journal of Hydraulic Engineering*, *137*(9), 995–1004. https://doi.org/10.1061/(ASCE)HY.1943-7900.0000377

Christiansen, T., Wiberg, P. L., & Milligan, T. G. (2000). Flow and sediment transport on a tidal salt marsh surface. *Estuarine, Coastal and Shelf Science*, *50*(3), 315–331. https://doi.org/10.1006/ecss.2000.0548

Corenblit, D., Tabacchi, E., Steiger, J., & Gurnell, A. M. (2007). Reciprocal interactions and adjustments between fluvial landforms and vegetation dynamics in river corridors: A review of complementary approaches. *Earth-Science Reviews*, *84*(1), 56–86. https://doi.org/10.1016/j.earscirev.2007.05.004

Cornacchia, L., Licci, S., Nepf, H., Folkard, A., Wal, D., Koppel, J., et al. (2018). Turbulence-mediated facilitation of resource uptake in patchy stream macrophytes. *Limnology and Oceanography*, *64*(2), 714–727. https://doi.org/10.1002/lno.11070

Costanza, R., d'Arge, R., De Groot, R., Farber, S., Grasso, M., Hannon, B., et al. (1997). The value of the world's ecosystem services and natural capital. *Nature*, *387*(6630), 253–260. https://doi.org/10.1038/387253a0

Dalrymple, R. A., Kirby, J. T., & Hwang, P. A. (1984). Wave diffraction due to areas of energy dissipation. *Journal of Waterway, Port, Coastal, and Ocean Engineering*, *110*(1), 67–79. https://doi.org/10.1061/(ASCE)0733-950X(1984)110:1(67)

de Langre, E., Gutierrez, A., & Cossé, J. (2012). On the scaling of drag reduction by reconfiguration in plants. *Comptes Rendus Mécanique*, *340*(1), 35–40. https://doi.org/10.1016/j.crme.2011.11.005

Etminan, V., Ghisalberti, M., & Lowe, R. J. (2018). Predicting bed shear stresses in vegetated channels. *Water Resources Research*, *54*, 9187–9206. https://doi.org/10.1029/2018WR022811

Etminan, V., Lowe, R. J., & Ghisalberti, M. (2017). A new model for predicting the drag exerted by vegetation canopies. *Water Resources Research*, *53*, 3179–3196. https://doi.org/10.1002/2016WR020090

Fathi-Maghadam, M., & Kouwen, N. (1997). Nonrigid, nonsubmerged, vegetative roughness on floodplains. *Journal of Hydraulic Engineering*, *123*(1), 51–57. https://doi.org/10.1061/(ASCE)0733-9429(1997)123:1(51)

Goring, D. G., & Nikora, V. I. (2002). Despiking acoustic Doppler velocimeter data. *Journal of Hydraulic Engineering*, *128*(1), 117–126. https://doi.org/10.1061/(ASCE)0733-9429(2002)128:1(117)

Gurnell, A. (2014). Plants as river system engineers. *Earth Surface Processes and Landforms*, *39*(1), 4–25. https://doi.org/10.1002/esp.3397

Harder, D., Speck, O., Hurd, C., & Speck, T. (2004). Reconfiguration as a prerequisite for survival in highly unstable flow-dominated habitats. *Journal of Plant Growth Regulation*, *23*(2), 98–107. https://doi.org/10.1007/s00344-004-0043-1

Hongwu, T., Wang, H., Liang, D. F., Lv, S. Q., & Yan, L. (2013). Incipient motion of sediment in the presence of emergent rigid vegetation. *Journal of Hydro-Environment Research*, *7*(3), 202–208. https://doi.org/10.1016/j.jher.2012.11.002

Huai, W., Zhang, J., Wang, W., & Katul, G. G. (2019). Turbulence structure in open channel flow with partially covered artificial emergent vegetation. *Journal of Hydrology*, *573*, 180–193. https://doi.org/10.1016/j.jhydrol.2019.03.071

Kaimal, J. C., & Finnigan, J. J. (1994). *Atmospheric boundary layer flows: Their structure and measurement*. New York, NY: Oxford University Press.

Kemp, J. L., Harper, D. M., & Crosa, G. A. (2000). The habitat-scale ecohydraulics of rivers. *Ecological Engineering*, *16*(1), 17–29. https://doi.org/10.1016/S0925-8574(00)00073-2

King, A. T., Tinoco, R. O., & Cowen, E. A. (2012). A *k*–ε turbulence model based on the scales of vertical shear and stem wakes valid for emergent and submerged vegetated flows. *Journal of Fluid Mechanics*, *701*, 1–39. https://doi.org/10.1017/jfm.2012.113

Kitsikoudis, V., Yagci, O., Kirca, V. S. O., & Kellecioglu, D. (2016). Experimental investigation of channel flow through idealized isolated tree-like vegetation. *Environmental Fluid Mechanics*, *16*(6), 1283–1308. https://doi.org/10.1007/s10652-016-9487-7

Kobayashi, N., Raichle, A. W., & Asano, T. (1993). Wave attenuation by vegetation. *Journal of Waterway, Port, Coastal, and Ocean Engineering*, *119*(1), 30–48. https://doi.org/10.1061/(ASCE)0733-950X(1993)119:1(30)

Lenhart, C. F. (2008). The influence of watershed hydrology and stream geomorphology on turbidity, sediment and nutrients in tributaries of the Blue Earth River. PhD thesis, University of Minnesota, USA.

Leonard, L. A., & Croft, A. L. (2006). The effect of standing biomass on flow velocity and turbulence in Spartina alterniflora canopies. *Estuarine, Coastal and Shelf Science*, *69*(3–4), 325–336. https://doi.org/10.1016/j.ecss.2006.05.004

Leonard, L. A., & Luther, M. E. (1995). Flow hydrodynamics in tidal marsh canopies. *Limnology and Oceanography*, *40*(8), 1474–1484. https://doi.org/10.4319/lo.1995.40.8.1474

Li, Y., Xie, L., & Su, T. C. (2020). Profile of suspended sediment concentration in submerged vegetated shallow water flow. *Water Resources Research*, *56*, e2019WR025551. https://doi.org/10.1029/2019WR025551

Lightbody, A. F., & Nepf, H. M. (2006). Prediction of velocity profiles and longitudinal dispersion in salt marsh vegetation. *Limnology and Oceanography*, *51*(1), 218–228. https://doi.org/10.4319/lo.2006.51.1.0218

Liu, C., Hu, Z., Lei, J., & Nepf, H. (2018). Vortex structure and sediment deposition in the wake behind a finite patch of model submerged vegetation. *Journal of Hydraulic Engineering*, *144*(2), 04017065. https://doi.org/10.1061/(ASCE)HY.1943-7900.0001408

Liu, J., Zhang, Z., Yu, Z., Liang, Y., Li, X., & Ren, L. (2017). The structure and flexural properties of *Typha* leaves. *Applied Bionics and Biomechanics*, *2017*, 1–9. https://doi.org/10.1155/2017/1249870

López, F., & García, M. (1998). Open-channel flow through simulated vegetation: Suspended sediment transport modeling. *Water Resources Research*, *34*(9), 2341–2352. https://doi.org/10.1029/98WR01922

Losada, I. J., Maza, M., & Lara, J. L. (2016). A new formulation for vegetation-induced damping under combined waves and currents. *Coastal Engineering*, *107*, 1–13. https://doi.org/10.1016/j.coastaleng.2015.09.011

Luhar, M., & Nepf, H. M. (2011). Flow-induced reconfiguration of buoyant and flexible aquatic vegetation. *Limnology and Oceanography*, *56*(6), 2003–2017. https://doi.org/10.4319/lo.2011.56.6.2003

López, F., & García, M. (2001). Mean flow and turbulence structure of open-channel flow through non-emergent vegetation. *Journal of Hydraulic Engineering*, *127*(5), 392–402. https://doi.org/10.1061/(ASCE)0733-9429(2001)127:5(392)

Maza, M., Adler, K., Ramos, D., Garcia, A. M. P., & Nepf, H. M. (2017). Velocity and drag evolution from the leading edge of a model mangrove forest. *Journal of Geophysical Research: Oceans*, *122*, 9144–9159. https://doi.org/10.1002/2017JC012945

Montakhab, A., Yusuf, B., Ghazali, A. H., & Mohamed, T. A. (2012). Flow and sediment transport in vegetated waterways: A review. *Reviews in Environmental Science and Bio/Technology*, *11*(3), 275–287. https://doi.org/10.1007/s11157-012-9266-y

Morris, E., Peralta, G., Brun, F., vanDuren, L., Bouma, T., & Perez-Llorens, J. (2008). Interaction between hydrodynamics and seagrass canopy structure: Spatially explicit effects on ammonium uptake rates. *Limnology and Oceanography*, *53*(4), 1531–1539. https://doi.org/10.4319/lo.2008.53.4.1531

Nepf, H. M. (1999). Drag, turbulence, and diffusion in flow through emergent vegetation. *Water Resources Research*, *35*(2), 479–489. https://doi.org/10.1029/1998WR900069

Nepf, H. M. (2012). Flow and transport in regions with aquatic vegetation. *Annual Review of Fluid Mechanics*, *44*(1), 123–142. https://doi.org/10.1146/annurev-fluid-120710-101048

Nepf, H. M., & Vivoni, E. R. (2000). Flow structure in depth-limited, vegetated flow. *Journal of Geophysical Research*, *105*(C12), 28,547–28,557. https://doi.org/10.1029/2000JC900145

Neumeier, U. (2007). Velocity and turbulence variations at the edge of saltmarshes. *Continental Shelf Research*, *27*(8), 1046–1059. https://doi.org/10.1016/j.csr.2005.07.009

Nikora, V., McEwan, I., McLean, S., Coleman, S., Pokrajac, D., & Walters, R. (2007). Double-averaging concept for rough-bed open-channel and overland flows: Theoretical background. *Journal of Hydraulic Engineering*, *133*(8), 873–883. https://doi.org/10.1061/(ASCE)0733-9429(2007)133:8(873)

Pearson, B. R., Krogstad, P.-Å., & van de Water, W. (2002). Measurements of the turbulent energy dissipation rate. *Physics of Fluids*, *14*(3), 1288–1290. https://doi.org/10.1063/1.1445422

Raupach, M. R., & Shaw, R. H. (1982). Averaging procedures for flow within vegetation canopies. *Boundary-Layer Meteorology*, *22*(1), 79–90. https://doi.org/10.1007/BF00128057

Rominger, J. T., Lightbody, A. F., & Nepf, H. M. (2010). Effects of added vegetation on sand bar stability and stream hydrodynamics. *Journal of Hydraulic Engineering*, *136*(12), 994–1002. https://doi.org/10.1061/(ASCE)HY.1943-7900.0000215

Sand-Jensen, K. (2003). Drag and reconfiguration of freshwater macrophytes. *Freshwater Biology*, *48*(2), 271–283. https://doi.org/10.1046/j.1365-2427.2003.00998.x

Stoesser, T., Kim, S. J., & Diplas, P. (2010). Turbulent flow through idealized emergent vegetation. *Journal of Hydraulic Engineering*, *136*(12), 1003–1017. https://doi.org/10.1061/(ASCE)HY.1943-7900.0000153

Tanino, Y. (2008). Flow and solute transport in random cylinder arrays: A model for emergent aquatic plant canopies (PhD thesis). MA, USA: Massachusetts Institute of Technology.

Tanino, Y., & Nepf, H. M. (2008). Lateral dispersion in random cylinder arrays at high Reynolds number. *Journal of Fluid Mechanics*, *600*, 339–371. https://doi.org/10.1017/S0022112008000505

Tennekes, H., & Lumley, J. L. (1972). *A first course in turbulence*. Cambridge, MA: MIT Press.

Termini, D. (2019). Turbulent mixing and dispersion mechanisms over flexible and dense vegetation. *Acta Geophysica*, *67*(3), 961–970. https://doi.org/10.1007/s11600-019-00272-8

Tinoco, R. O. (2011). An experimental investigation of drag and the turbulent flow structure in simulated and real aquatic vegetation (PhD thesis). NY, USA: Cornell University.

Tinoco, R. O., & Coco, G. (2016). A laboratory study on sediment resuspension within arrays of rigid cylinders. *Advances in Water Resources*, *92*, 1–9. https://doi.org/10.1016/j.advwatres.2016.04.003
Tinoco, R. O., & Coco, G. (2018). Turbulence as the main driver of resuspension in oscillatory flow through vegetation. *Journal of Geophysical Research: Earth Surface*, *123*, 891–904. https://doi.org/10.1002/2017JF004504
Tsujimoto, T. (1999). Fluvial processes in streams with vegetation. *Journal of Hydraulic Research*, *37*(6), 789–803. https://doi.org/10.1080/00221689909498512
Uittenbogaard, R. E. (2003). Modelling turbulence in vegetated aquatic flows, paper presented at International Workshop on Riparian Forest Vegetated Channels: Hydraulic, morphological and ecological aspects, RIPFOR, Trento, Italy.
Vogel, S. (1989). Drag and reconfiguration of broad leaves in high winds. *Journal of Experimental Botany*, *40*(8), 941–948. https://doi.org/10.1093/jxb/40.8.941
Wang, H., Tang, H., Zhao, H., Zhao, X., & Lü, S. (2015). Incipient motion of sediment in presence of submerged flexible vegetation. *Water Science and Engineering*, *8*(1), 63–67. https://doi.org/10.1016/j.wse.2015.01.002
White, F. M. (1991). *Viscous fluid flow* (second ed., 614 pp.). New York, NY: McGraw-Hill.
Wilcock, R. J., Champion, P. D., Nagels, J. W., & Croker, G. F. (1999). The influence of aquatic macrophytes on the hydraulic and physico-chemical properties of a New Zealand lowland stream. *Hydrobiologia*, *416*(0), 203–214. https://doi.org/10.1023/A:1003837231848
Wilson, N. R., & Shaw, R. H. (1977). A higher order closure model for canopy flow. *Journal of Applied Meteorology*, *16*(11), 1197–1205. https://doi.org/10.1175/1520-0450(1977)016<1197:AHOCMF>2.0.CO;2
Yagci, O., Tschiesche, U., & Kabdasli, M. S. (2010). The role of different forms of natural riparian vegetation on turbulence and kinetic energy characteristics. *Advances in Water Resources*, *33*(5), 601–614. https://doi.org/10.1016/j.advwatres.2010.03.008
Yager, E. M., & Schmeeckle, M. W. (2013). The influence of vegetation on turbulence and bed load transport. *Journal of Geophysical Research: Earth Surface*, *118*, 1585–1601. https://doi.org/10.1002/jgrf.20085
Yang, J. Q., Chung, H., & Nepf, H. M. (2016). The onset of sediment transport in vegetated channels predicted by turbulent kinetic energy. *Geophysical Research Letters*, *43*, 11,261–11,268. https://doi.org/10.1002/2016GL071092
Zhang, Z., & Nepf, H. (2020). Flow-induced reconfiguration of aquatic plants, including the impact of leaf sheltering. *Limnology and Oceanography*, 1–16. https://doi.org/10.1002/lno.11542
Zhang, Y., Tang, C., & Nepf, H. (2018). Turbulent kinetic energy in submerged model canopies under oscillatory flow. *Water Resources Research*, *54*, 1734–1750. https://doi.org/10.1002/2017WR021732

References From the Supporting Information

Kundu, P. K., & Cohen, I. M. (2008). *Fluid mechanics* (4th ed.). San Diego, CA: Academic Press.
Liu, D., Diplas, P., Fairbanks, J. D., & Hodges, C. C. (2008). An experimental study of flow through rigid vegetation. *Journal of Geophysical Research*, *113*, F04015. https://doi.org/10.1029/2008JF001042
Tanino, Y., & Nepf, H. M. (2007). Experimental investigation of lateral dispersion in aquatic canopies, paper presented at 32nd Congress-International Association for Hydraulic Research, p. 152, Venice, Italy, 1–6 Jul.